Int J Adv Manuf Technol (2018) 95:2059–2070
https://doi.org/10.1007/s00170-017-1340-8

ORIGINAL ARTICLE

Effects of material properties on warpage in fused deposition modeling parts

Emily R. Fitzharris[1] · **Narumi Watanabe**[2] · **David W. Rosen**[2,3] · **Meisha L. Shofner**[1,4]

Received: 5 July 2017 / Accepted: 7 November 2017 / Published online: 18 November 2017

Abstract Fused deposition modeling (FDM) offers many advantages over conventional manufacturing methods, but it is limited by the number of materials available. Extending FDM technology to semicrystalline polymers has been challenging due to the crystallization that occurs during cooling which results in FDM part warpage. Previous work used process simulation models to study the effects of material parameters and FDM process variables on the part warpage seen using polypropylene (PP). In this work, the process simulation models were adapted to investigate warpage of FDM parts made with a high-performance semicrystalline polymer, polyphenylene sulfide (PPS). Material parameters in the PPS process simulation models were individually changed to the PP values to investigate which material parameters cause PP to exhibit higher warpage than PPS. Material parameters of interest included coefficient of thermal expansion (CTE), thermal conductivity, heat capacity, and Young's modulus. Additional material parameters based on material property modification through the addition of fillers were investigated in order to establish the relationship between material parameters and warpage values. The simulation models suggested that the CTE has the largest impact on FDM part warpage. Decreasing the CTE in the simulation model resulted in a decrease in the FDM part warpage by the same factor.

Keywords Additive manufacturing · Fused deposition modeling · Polyphenylene sulfide · Coefficient of thermal expansion · Shrinkage

✉ Meisha L. Shofner
meisha.shofner@mse.gatech.edu

[1] School of Materials Science and Engineering, Georgia Institute of Technology, 801 Ferst Drive, Atlanta, GA 30332-0295, USA

[2] George W. Woodruff School of Mechanical Engineering, Georgia Institute of Technology, 801 Ferst Drive, Atlanta, GA 30332-0405, USA

[3] Digital Manufacturing and Design Centre, Singapore University of Technology and Design, 8 Somapah Road, Singapore 487372, Republic of Singapore

[4] Renewable Bioproducts Institute, Georgia Institute of Technology, 500 10th Street NW, Atlanta, GA 30332-0620, USA

1 Introduction

Additive manufacturing (AM) is a class of manufacturing techniques in which three-dimensional parts are constructed in an additive, layer-by-layer fashion. In AM, a 3D computer-aided design (CAD) model of the desired part is constructed. The CAD representation is then converted into an STL file, which is then "sliced" into thin, horizontal layers in the XY plane using AM slicing software packages. The slicing software also generates a toolpath for the AM machine to follow in order to construct the original 3D geometry one layer at a time [1–3]. There are several different types of AM processes such as stereolithography (SLA), fused deposition modeling (FDM), selective laser sintering (SLS), and material jetting. These methods vary based on the precursor materials and the mechanisms they utilize to fabricate 3D parts layer-by-layer.

FDM is an AM process used to fabricate three-dimensional parts through layer-by-layer deposition of liquefied thermoplastic filament. Fabricating a 3D part with FDM follows the general procedure outlined for AM previously. Once the CAD file is converted to an STL file and sliced using the AM slicing software, the FDM machine follows the generated toolpath to fabricate the part from the bottom up. Layers are fabricated by translating a polymer filament through a liquefier chamber and extruding it out of a nozzle where it is deposited as roads in positions on the XY plane according to the toolpath. Once

all the roads in a layer are deposited, the FDM build platform moves downward in the z direction to allow the next layer to be built on top of the previous layer. Throughout fabrication, the three-dimensional part experiences cycles of heating and cooling as subsequent roads are deposited on cooled layers.

FDM offers advantages over conventional manufacturing methods for several reasons which are common to many additive manufacturing technologies. It can fabricate more complex geometries than traditional machining and molding operations, and its additive as opposed to subtractive nature provides a capability to use less material to produce a given part. However, a limited number of materials for FDM limits the range of applications for the process, whereas traditional manufacturing methods can accommodate a large library of materials.

The most commonly used polymer with FDM, acrylonitrile-*co*-butadiene-*co*-styrene (ABS), is an amorphous and rigid engineering thermoplastic copolymer, and it has many properties that are useful for producing prototypes and end-use parts for some applications. Some of these useful properties include low cost, durability, and toughness [4–6]. FDM could be extended to additional production applications by using precursor polymers with the structural or functional properties desired in the part. Among these possible materials are semicrystalline polymers. Semicrystalline polymers offer advantages over amorphous polymers because they are deformable, tough, and in general, have higher service temperatures than amorphous polymers [7, 8]. Semicrystalline polymers present challenges in FDM processing due to the shrinkage that occurs during part cooling and crystallization. During crystallization, polymer chains are drawn together as they order to form more dense, crystalline regions. This ordering results in increased part shrinkage when compared to parts fabricated with amorphous thermoplastic polymers. Shrinkage also occurs to a lesser extent in amorphous materials, and one way that this behavior is characterized in polymers is with their coefficient of thermal expansion (CTE) value. Increased shrinkage is also an issue in molding operations with semicrystalline polymers, but mold cavity sizes can be designed to adequately account for the expected material shrinkage [9]. Specifically in FDM, the formation of the crystalline structure in polymers results in parts that warp and become detached from the build platform during FDM part fabrication, resulting in difficulty in fabrication and reduced part quality. This part warpage is shown schematically in Fig. 1.

Aside from the use of semicrystalline polymers, another method used to extend FDM to part production is to use fillers to increase material properties in polymer systems that are compatible with the FDM process. The tensile strength, modulus, and/or thermal conductivity of ABS have been increased through the addition of fillers such as carbon nanofiber, carbon fiber, glass fiber, and metallic particles [10–14]. The

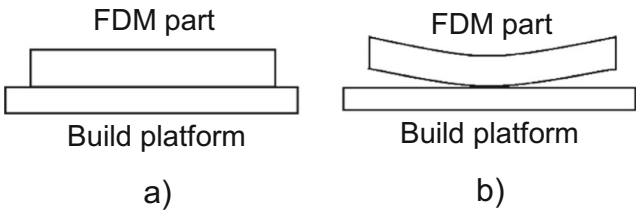

Fig. 1 Representation of part warpage and shrinkage seen in FDM parts fabricated with **a** amorphous thermoplastic polymers and **b** semicrystalline thermoplastic polymers. Shrinkage that results from polymer chains drawing together and ordering during crystallization causes FDM parts to warp and separate from the build platform when printing semicrystalline polymers

material properties of other semicrystalline polymer systems, such as polypropylene (PP) and poly(ε-caprolactone) (PCL), have been similarly modified using fillers such as thermotropic liquid crystalline polymers, bioactive glass, and glass fiber for use with FDM [15–19].

While the aforementioned studies focused primarily on enhancing the material properties of the FDM feedstock in order to increase the mechanical properties of the resulting FDM parts, others have used the addition of fillers to various polymer systems to improve the actual FDM process itself. Residual stresses and part warpage due to thermal gradients within FDM parts present challenges during the manufacturing of parts with FDM using both amorphous and semicrystalline materials. Previously, these challenges have been addressed by manufacturing FDM parts in a heated chamber to reduce the thermal gradients experienced by the parts. Love et al. showed that the addition of carbon fiber to ABS improved the strength and stiffness of final FDM parts. In addition, the carbon fiber increased the thermal conductivity and decreased the CTE of ABS. The changes in thermal conductivity and CTE led to reduced distortion or warpage in the FDM parts, especially in large-scale manufacturing of FDM parts [20].

This same concept was also applied to a semicrystalline polymer, polyphenylene sulfide (PPS) [21]. This work used a lab-scale FDM machine developed specifically to process high temperature and high fiber content thermoplastic polymer pellets. This system differs from standard FDM machines that use thermoplastic filament as the precursor material. The addition of carbon fiber to PPS led to increased thermal conductivity and decreased CTE as seen in ABS. In addition, the carbon fiber reduced the die swell seen in PPS when extruded from the FDM nozzle, slowed down crystallization processes (both from the melt and upon heating, i.e., cold crystallization), and reduced the overall crystallinity of the composite. Because of these changes seen in the composite, large-scale PPS parts could be fabricated without significant part warpage using FDM with an environment at room temperature. In another case, aluminum oxide and aluminum nanofillers were used to reduce the crystallinity, reduce the melt flow index,

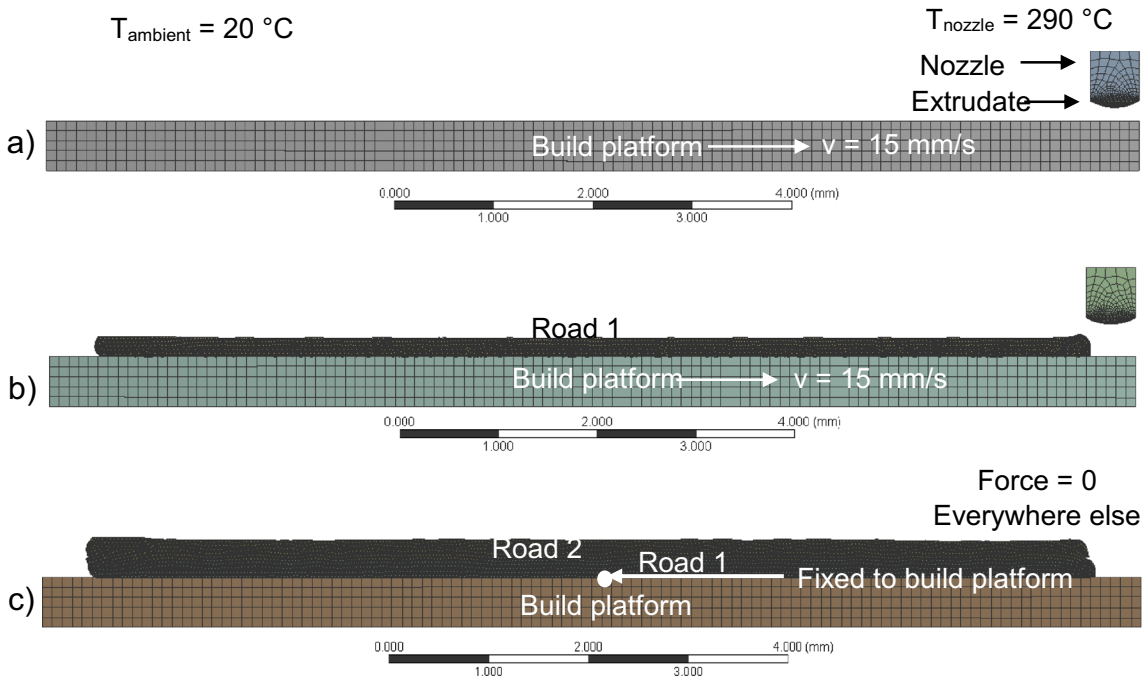

Fig. 2 The mesh and simulation set up before road 1 deposition are shown in **a**. Adaptive meshing is applied in the extrudate in order to properly mesh the rapidly changing geometry in road 1 during its deposition. The final geometry and mesh in road 1 after its deposition is shown in **b**. This geometry and mesh were imported and used during road 1 cooling. Road 2 was deposited on top of this mesh and geometry. The mesh and geometry of roads 1 and 2 are shown in **c**. These final meshes were used in the warpage and residual stresses simulation in which road 1 was assumed to be fixed to the build platform at a center point shown in **c**

and increase the thermal properties of polyamide 6 to make it compatible with the FDM process [22].

Previous work by the authors investigated FDM of an inexpensive and flexible semicrystalline thermoplastic, polypropylene (PP) [23]. The effects of material properties and process variable settings of FDM were examined using experiments and a multistep simulation model that simulated the deposition and cooling of two FDM filament roads. The results of that work indicated that some reductions in part warpage could be realized by changing process variables. Specifically, part warpage was reduced with increased deposition speed and increased layer height. Beyond process variables, material properties could be changed to reduce the warpage of PP parts, namely the introduction of fillers or the use of a less crystalline polymer such as propylene copolymers. Experimental results agreed qualitatively with the results obtained from the simulation model and showed that part warpage was influenced by material properties. Specifically, materials with a reduced CTE and/or an increased thermal conductivity showed reduced warpage.

In this paper, neat PPS is investigated as a material for FDM using the same simulation model that the authors used to understand the printing behavior of PP. PPS is a high-performance semicrystalline thermoplastic known for its chemical and temperature resistance [24, 25]. Due to the high melting temperature of PPS, the FDM processing temperature for PPS is higher than the temperature for PP, 290 vs. 220 °C, respectively. This higher processing temperature results in faster convective cooling with the environment and could cause increased thermal gradients in the FDM part and, based on previous studies, suggests that PPS could exhibit increased warpage as compared to PP. However, PPS parts produced by the authors exhibit very little warpage when fabricated using FDM, especially compared to the warpage seen in unmodified PP. Therefore, the objective of this study was to identify what material properties of PPS caused it to exhibit minimal warpage when compared to PP through the use of a process simulation model. Material parameters of PPS were parametrically changed to understand more fully which material properties have the largest effect on part warpage.

2 Methods

2.1 Process simulation model

The process simulation model used in this work was described previously in Watanabe et al. [23]. The model used coupled simulations in ANSYS® Polyflow and ANSYS® Mechanical to analyze the FDM process from the liquefaction step to the deposition and cooling steps, examining the effects of material and process parameters on PP part warpage. Multiple simulation models were used to represent the thermal and mechanical processes experienced during FDM part fabrication. In this

work, these models were modified to study PPS. The previous simulation was adapted to simulate the higher FDM extrusion temperature required for PPS, a higher build platform temperature, and a longer deposition length.

In the FDM process simulation models, 2–10-mm-long roads of PPS filament were deposited at 290 °C onto a build platform held at a constant temperature of 85 °C. These temperatures were chosen since they matched the experimental values used to print PPS with FDM. The build platform was assumed to be glass and had a heat transfer coefficient of 100 W/m^2-°C to match the experimental FDM set up. The FDM process was broken down into five sequential simulation models: road 1 deposition, road 1 cooling, road 2 deposition, road 1 and 2 cooling, and residual stress and warpage analysis. These simulation models were linked together by importing the geometry and temperature profile from the previous model into the current model as the simulation progressed through the FDM process. Figure 2 shows the meshes used in these simulation models.

In the first simulation model, a road of PPS was deposited through an extrusion nozzle onto the build platform at a volumetric flow rate determined by Eq. 1:

$$Q = v_r WH \tag{1}$$

where v_r was the deposition velocity, W was the width of the deposited rectangular road, and H was the road height. While the nozzle used in FDM had a round orifice, the deposited road adopted an approximately rectangular shape, so that shape was used in this calculation [26]. During the simulated deposition, the PPS filament was extruded through the nozzle in the vertical direction by applying the volumetric flow rate at the nozzle entrance with a gravitational force to cause the extrudate to flow downward from the nozzle. The nozzle was held in a stationary position as the build platform translated horizontally at the deposition speed of 15 mm/s. This deposition speed is similar to the speed used with the FDM machine for experimental work in this study. As the first road was deposited on the build platform, the mesh in the extrudate deformed significantly. In order to properly mesh the changing geometry seen in the first road deposition, the remeshing technique in ANSYS® Polyflow was applied to the extrudate at the nozzle entrance to continually refresh the mesh in the first road during its deposition. The meshes applied to the build platform, nozzle, and extrudate before layer 1 deposition are shown in Fig. 2a.

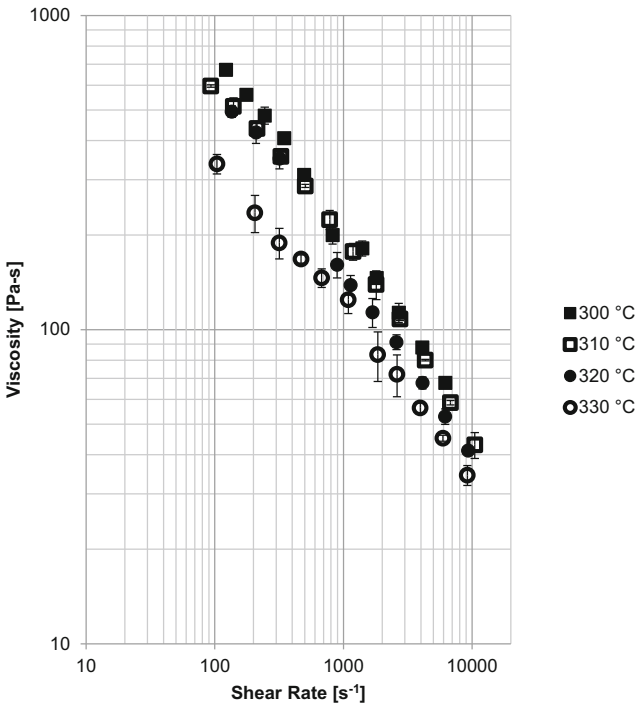

Fig. 3 The viscosity of PPS as a function of shear rate. Viscosity decreases with increasing shear rate and increasing temperature as expected

The geometry and temperature profile of the first road were exported and used in the first road cooling model. In this model, the build platform temperature was applied to the bottom surface of the first road while the outer surfaces were subjected to convective cooling with air at an ambient temperature of 20 °C. The mesh and geometry used in this step are shown in Fig. 2b. The cooling simulation was run over a time equal to the deposition time plus 1 s. The deposition time corresponded to the horizontal movement of the build platform back to its original position, and the 1 s corresponded to the time required for the vertical movement of the build platform downward to prepare for the second road deposition.

Second road deposition and cooling proceeded in a manner very similar to the first road deposition and cooling. The second road was deposited on top of the first road that was characterized by the exported geometry and temperature profile from the previous simulation model. During the second road deposition, conductive heat transfer occurred between the two roads by utilizing the fluid-to-fluid contact capability in ANSYS® Polyflow. The second road was then allowed to cool for 10 s. The geometries and final meshes in the first and second roads are shown in Fig. 2c. During this cooling period, the residual stress and warpage seen in the two roads were analyzed in the final simulation model.

The temperature profiles and geometries of the two roads were exported from the roads 1 and 2 cooling simulation model and imported into ANSYS® Mechanical to conduct structural analysis in the final process simulation model. The midpoint of the first road was fixed to the build platform, and a zero force was applied everywhere else in order to compute the residual stress and warpage experienced in the two roads during cooling. The location of the fixed point between the first road and the build platform is shown in Fig. 2c.

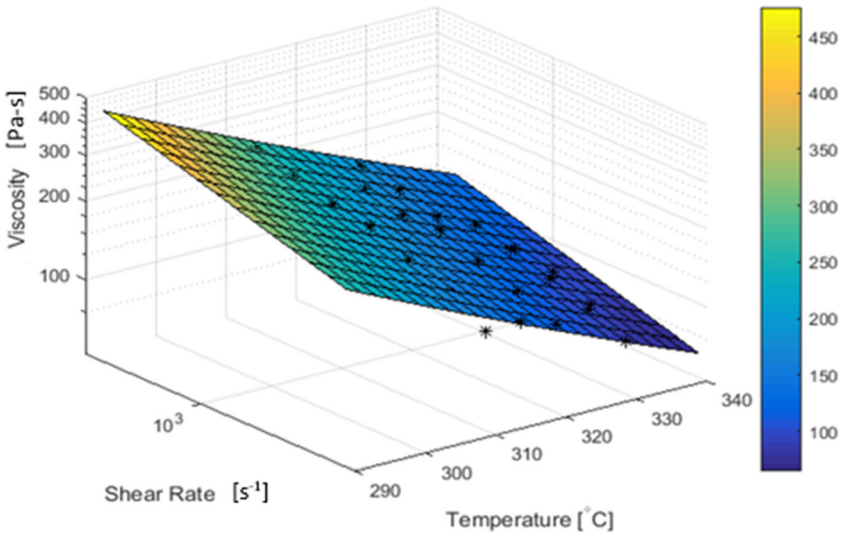

Fig. 4 A viscosity surface plot for PPS was constructed by fitting Eq. 4 to the experimental data. The symbols (*) represent experimental data while the surface plot was obtained using Eq. 4, which was used to plot viscosity as a function of shear rate and temperature from 290 to 340 °C and from 100 to 10,000 s^{-1}

2.2 Material properties

The wide range of temperatures that occur during FDM made it necessary to consider many material parameters as a function of temperature [3]. To obtain inputs for the simulation model, the flow characteristics of PPS were characterized using both a theoretical treatment and experimental data from capillary rheology.

The dependence of PPS viscosity on both shear rate and temperature was accounted for in the FDM process by using the power-law viscosity model shown in Eq. 2:

$$\eta = K\left(\dot{\gamma}\right)^{n-1} \tag{2}$$

where η is viscosity, $\dot{\gamma}$ is shear rate, and K and n are power-law fit parameters. The temperature dependence of the viscosity was assumed to be described by an Arrhenius model shown in Eq. 3:

$$H(T) = e^{\left[\alpha\left(\frac{1}{T}-\frac{1}{T_0}\right)\right]} \tag{3}$$

where α is the activation energy and T_0 is the reference temperature. The final viscosity equation for PPS combined the dependence of viscosity on shear rate and the dependence of viscosity on temperature [27]. This expression is given in Eq. 4.

$$\eta = H(T)\eta_{T_0}\left(\dot{\gamma}\right) \tag{4}$$

Experiments were conducted on a capillary rheometer, the Dynisco LCR7001 [28], at various shear rates and temperatures to obtain a viscosity expression for PPS according to the equations given above. The L/D ratio of the capillary die was 40 with a length of 20 mm and a diameter of 0.5 mm. Shear rates representative of the FDM process, 100 to 10,000 s^{-1} [3, 16], were used at temperatures 300, 310, 320, and 330 °C. PPS pellets used in the experimental runs were obtained from Technical Polymers with the product name Thermec S™. Two experimental runs were conducted at each temperature and a correction was made to convert apparent viscosity to true viscosity. No Bagley correction was performed due to limited capillary dies available for use. The viscosity as a function

Table 1 Material properties of PPS and PP used in the simulation models [23, 29, 30]

Material property	PPS	PP
Viscosity expression	$\eta = e^{\left[9345.5\left(\frac{1}{T}-\frac{1}{593.15}\right)\right]}914.61\left(\dot{\gamma}\right)^{-0.25}$	$\eta = e^{\left[1318.9\left(\frac{1}{T}-\frac{1}{503.15}\right)\right]}3346.4\left(\dot{\gamma}\right)^{-0.54}$
Density	1350 kg/m^3	900 kg/m^3
Coefficient of thermal expansion	5.04×10^{-5} m/(m-°C)	1.5×10^{-4} m/(m-°C)
Thermal conductivity	0.288 W/(m-°C)	0.2 W/(m-°C)
Heat capacity per unit mass	1001 J/(kg-K)	1920 J/(kg-K)
Surface tension coefficient	38 mJ/m^2	30.5 mJ/m^2
Young's modulus	4.5 GPa	1.75 GPa
Poisson's ratio	0.38	0.38

Table 2 Process variable settings for process simulation models [23]

Process variable setting	PPS	PP
Environmental temperature	20 °C	
Deposition temperature	290 °C	220 °C
Build platform temperature	85 °C	80 °C
Deposition length	10 mm	5 mm
Deposition speed	15 mm/s	20 mm/s
Layer height	0.2 mm	

of shear rate obtained from experiments at each temperature is shown in Fig. 3. The viscosity equation given in Eq. 4 was fit to the experimental data. Using this equation, a viscosity surface plot was constructed to show the viscosity as a function of shear rate and temperature over a larger temperature range. This surface plot is shown in Fig. 4.

Table 1 shows the material properties of PPS used as inputs for the simulation models compared to the same values for PP used in previous work [23]. Most of these values were obtained from general material data sheets as opposed to experiment and may not exactly represent the properties of the materials or temperatures used for validation studies. Therefore, the simulation results were used primarily as qualitative indicators of material behavior and to provide a basis for comparison between the two polymers. Additionally, the volume contraction during crystallization was not captured explicitly in the simulation. Instead, CTE was used to describe the differences between the materials. Future work may be modified to obtain more quantitative results.

In this work, the 2D simulation models by Watanabe et al. to model PP parts fabricated with FDM were modified in order to model PPS FDM parts [23]. The deposition temperature, deposition length, deposition speed, build platform temperature, and material parameters were modified in order to simulate the deposition of PPS in FDM. Due to the dramatic decrease in part warpage seen in the PPS simulation model, material parameters of PPS were then individually changed to values of PP to examine the effects of material parameters on part warpage in FDM part fabrication.

2.3 FDM additive manufacturing machine

The FDM additive manufacturing machine used in this work to validate the results of the process simulation models was the HYREL System 30 from HYREL 3D [31]. The open hardware and software in the HYREL System 30 give users a large amount of control over the FDM process. The extrusion head and heated build platform are enclosed in a build chamber to keep the environmental conditions stable. The extrusion head used in this work could accommodate temperatures from 250 to 450 °C and used a spring mounted roller to translate the FDM filament into the liquefier chamber. The spring mounted roller allowed for filaments with varying diameters to be translated into the chamber without clogging or stalling. The hardware used a modified version of the Repetier [32] controller software, known as Repetrel, created by Hyrel. Within Repetrel, various process settings such as extrusion temperature, build platform temperature, filament feed rate, and the nozzle z position could be adjusted in real time during part fabrication. Repetrel instructed the print head where to deposit filament based on CAD models through toolpath information in a G-Code file. The G-Code used in Repetrel was written using the common slicing CAD software slic3r [33]. Slic3r had a variety of adjustable settings such as layer height, deposition speed, solid/infill patterns, and more that control how a CAD model was realized through the deposition of liquefied filament in the FDM machine. Validation parts were constructed using PP FDM filament obtained from Gizmo Dorks and PPS monofilament.

Since Watanabe et al. showed that process variable settings, such as deposition speed and layer height, affected part warpage in PP [23], a consistent set of process variables was used in the simulation and experimental work. The values of those

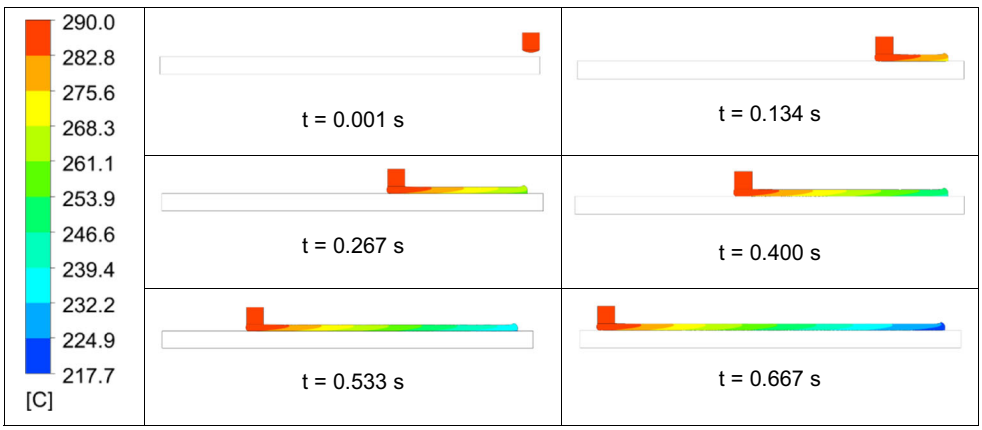

Fig. 5 Temperature distribution and filament shape during road 1 deposition of PPS. As road 1 is deposited, it experiences convective cooling with the environment at 20 °C and conductive cooling with the build platform at 85 °C

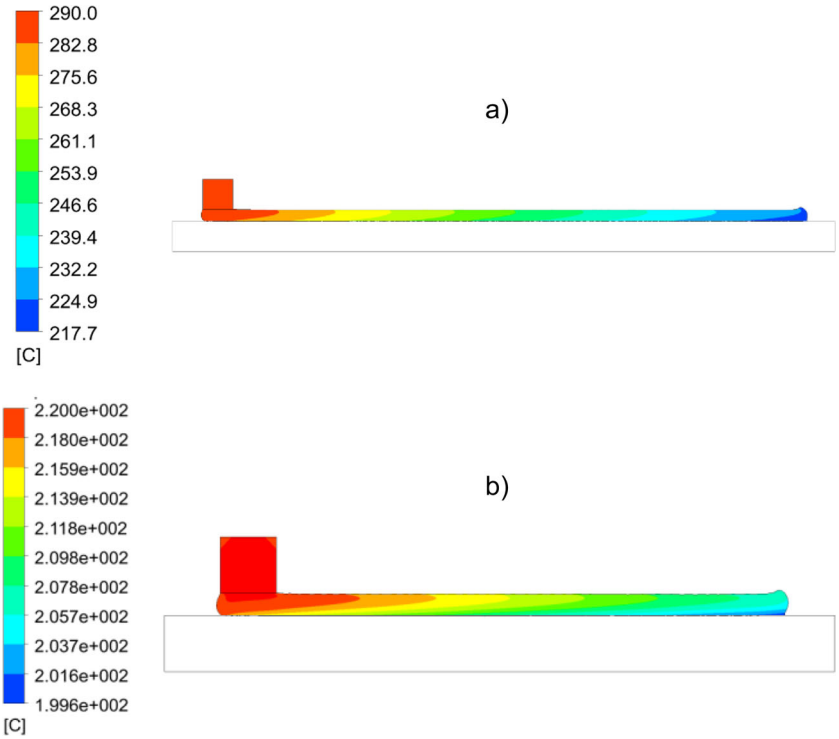

Fig. 6 Final geometry and temperature distribution in road 1 deposition for **a** PPS and **b** PP [23]. The higher extrusion temperature, longer deposition length, and slower deposition speed used with PPS result in a larger temperature gradient in the PPS road 1

process variables are given in Table 2. PPS and PP parts were fabricated using the process variables in Table 2. A slower deposition speed than that used for PP was chosen to reduce drool and improve surface finish. The deposition temperature was increased from 220 to 290 °C to accommodate the higher melting temperature of PPS, 280 °C, and the build platform temperature was increased from 80 to 85 °C. The deposition length was increased to 10 mm to better represent the scale of typical FDM parts without significantly increasing the computation time of the simulation models. Significantly larger deposition lengths would have resulted in much larger simulation model computation times.

3 Results

3.1 PPS simulation model and experimental validation

The sequential simulation models demonstrated the FDM process of PPS. Figure 5 shows the temperature distribution and shape of the first road as it was deposited on the build platform in the first simulation model. Due to the higher deposition temperature used with PPS in this simulation model, the thermal gradients present in the first road deposition were larger than the thermal gradients when depositing PP in previous work. The slower deposition speed, 15 versus 20 mm/s, resulted in a longer deposition time. This contributed to an increase in thermal gradients in the road. The longer deposition length, 10 versus 5 mm, also resulted in a longer deposition time, allowing deposited sections more time to cool during the deposition step. The final result of the first road deposition of PP is compared to PPS in Fig. 6. Table 3 shows the differences in temperatures seen in the first road deposition.

Table 3 Temperatures seen in road 1 deposition in PPS and PP simulation models [23]

Temperature	PPS	PP
T_{max}	290.0 °C	220.0 °C
T_{min}	217.7 °C	199.6 °C
ΔT	72.3 °C	20.4 °C

During the cooling step, the first layer cooled for 1.67 s during which the build platform moved horizontally back to its original position and indexed downward to prepare for the second road deposition. The deposition nozzle was not in contact with the road during cooling. The first road was deposited at 290 °C and cooled to approximately 100 °C in 0.239 s. In the previous study with PP, the first road was deposited at 220 °C and cooled to approximately 122 °C in 0.25 s [23]. The faster cooling seen in PPS is due to the larger difference between the deposition temperature and the environmental temperature.

The temperature distributions and filament shapes during the second road deposition and roads 1 and 2 cooling are shown in Figs. 7 and 8, respectively. The procedure for this simulation model was similar to the procedure described for

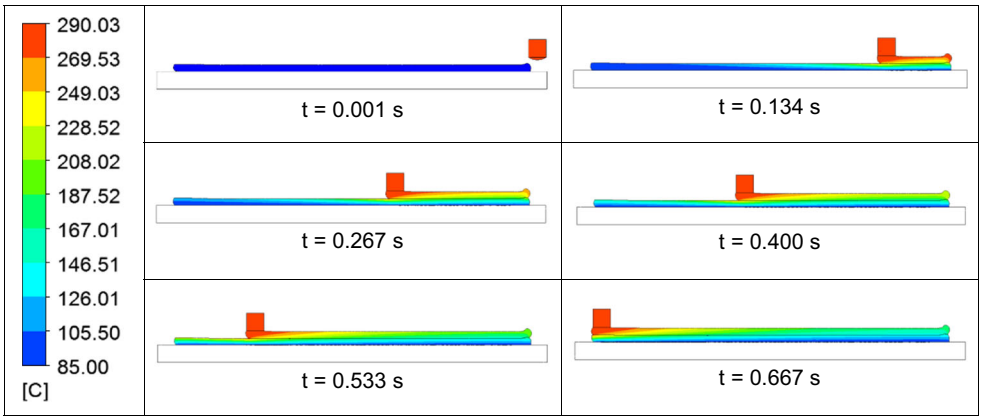

Fig. 7 Temperature distribution and road geometries during road 2 deposition of PPS. Road 2 deposition begins with a completely cooled road 1 at 85 °C. When road 2 makes contact with road 1, conductive heat transfer occurs between the two roads and road 1 increases in temperature. As the deposition proceeds, the two layers begin to cool together through convective cooling with the environment and conductive cooling with the build platform

the first road deposition and cooling. During the second road deposition, conductive heat transfer occurred between road 1 and road 2. The two roads were then allowed to cool for 10 s to allow the roads to cool completely from their deposition.

The last simulation model was performed in ANSYS® Mechanical to predict the thermally induced residual stresses and part warpage caused by the crystallization of the material during cooling. During road 2 deposition, road 1 was reheated as it came in contact with road 2 as shown in Fig. 7. Road 2 and the reheated road 1 then cooled together and crystallized causing warpage and simultaneously inducing residual stresses. The part warpage and residual stresses of the two deposited roads are shown in Figs. 9 and 10, respectively. In Fig. 9, the part warpage is shown in the two roads by measuring the deformation of the edges of the road from the build platform. At the edges, PPS showed a warpage of 0.017 mm. The inset in Fig. 9 shows the warpage to scale while the main figure is shown at a magnified scale so that the shape produced by the warpage can be visualized. Figure 10 shows that minimal residual stresses were developed in the PPS roads during cooling. As a result, little warpage was observed, especially when compared to the warpage of 0.100 mm exhibited by PP in previous work by Watanabe et al. [23].

Because the process simulation models were computationally intensive, only two layers that were 10 mm long were simulated. In order to validate the model, PPS FDM parts were fabricated using the HYREL System 30. The fabricated parts were 0.4 mm tall and 0.5 mm wide and were made using two 0.2-mm-tall layers to match the process simulation models. They were fabricated with several lengths including 10, 20, 40, and 80 mm. The 10-mm-long road matched the geometry that was modeled using the PPS process simulation models. Additional geometries were fabricated with PPS and PP to match the experimental validation used by Watanabe et al. [23]. The geometry in that work was a 20 mm by 20 mm rectangle that was 1 mm tall (5 layers). The different part lengths led to differences in absolute warpage values between the process simulation models and the fabricated parts, so the warpage values determined from the process simulation model were extrapolated to longer deposition lengths.

This extrapolation was performed by assuming that the radius of curvature of the part was constant. The radius of curvature, r, was calculated using Eq. 5:

$$r = \frac{H}{2} + \frac{W^2}{8H} \tag{5}$$

where W is the deposition length and H is the warpage calculated using the process simulation models. The radius of curvature was calculated for PPS and PP using the warpage results obtained from the process simulation models [23]. These radii were then used to calculate the warpage for varying deposition lengths. The larger radius of curvature for PPS

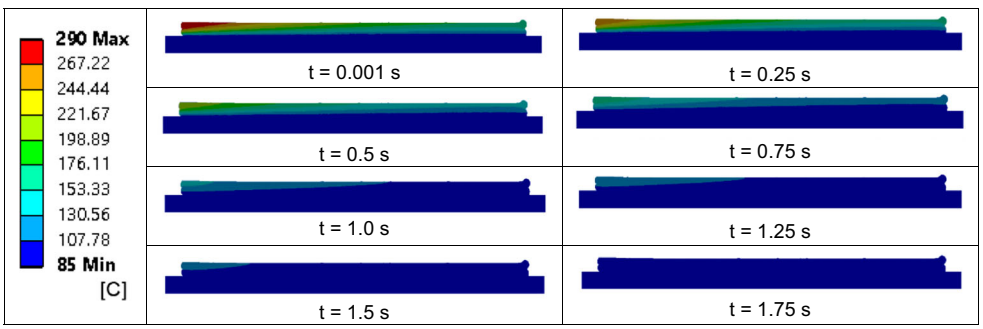

Fig. 8 Temperature distribution during roads 1 and 2 cooling of PPS. After road 2 deposition, the deposition nozzle moves off the geometry and the two roads begin cooling together through convective cooling with the environment and conductive cooling with the build platform. The roads are allowed to cool for 10 s, but they cool completely in 1.75 s

Fig. 9 Warpage exhibited by PPS in the process simulation model. PPS roads 1 and 2 exhibit a warpage of 0.017 mm after cooling together for 10 s. The inset shows the geometry to scale while the main figure is scaled by a factor of 10 to show the shape the warpage exhibits

corresponded to lower warpage values when compared to the smaller radius of curvature of PP. The simulation models predicted that for a 10-mm-long part, PPS would warp 0.017 mm while PP would warp 0.100 mm. Following the simulation model predictions, a 40-mm-long PPS part with two layers should warp 0.270 mm and a PP should warp 1.537 mm. Additional layers would cause these warpage values to increase.

As previously described, warpage experienced by FDM parts causes them to separate from the build platform during fabrication. This behavior was observed by Watanabe et al. [23]. However, when fabricating PPS parts with FDM, no warpage was visible for any of the fabricated geometries and the entire part remained completely adhered to the build platform. This implied that there were minimal residual stresses present in the fabricated part, which was consistent with the results obtained by the process simulation model. A 20 mm by 20 mm by 1 mm PPS part that was fabricated is shown in Fig. 11. The figure shows that the part did not warp or detach from the build platform during printing. For comparison, a 20 mm by 20 mm by 1 mm PP part was also fabricated. As shown in Fig. 11, the part detached from the build platform during printing, implying that there were residual stresses present in the part. These results are consistent with what was observed previously [23].

3.2 Parametric studies based on material parameters

The parametric studies of the warpage simulation model were conducted by changing the material parameters in the PPS model to determine which material properties affected part warpage. Values for PP were used in addition to other logical values. The material parameters of interest were CTE, thermal conductivity, heat capacity, and Young's modulus. Table 4 shows the warpage value obtained from the PPS process simulation models with varied material parameters and how those material parameters compare to the original PPS value. It also shows the comparison of the warpage values from the warpage value of 0.017 mm obtained using the base PPS process simulation models.

The CTE showed direct scaling with the warpage value in the process simulation models. In the PPS process simulation models, when the CTE was increased by a factor of 2.98, the warpage value obtained also increased by a factor of 2.98. Changing the thermal conductivity, heat capacity, and Young's modulus by factors of 0.69, 1.92, and 0.39, respectively, did not significantly affect the warpage seen in the process simulation models. The warpage vs. deposition length plots for PP, PPS, and the PPS process simulation with a modified CTE value are shown in Fig. 12.

The effects of changing multiple material parameters at once were studied using different combinations of CTE, thermal conductivity, and heat capacity values in the PPS process simulation model. Table 5 shows the warpage value obtained for the simulations along with how it compares to the warpage value from the base PPS process simulation models.

As seen in Table 5, some material parameters have a more significant effect on warpage when changed in

Fig. 10 Residual stresses in roads 1 and 2 at steady state. PPS roads 1 and 2 exhibit minimal residual stress after cooling. The inset shows the geometry to scale while the main figure is scaled by a factor of 10 to show the shape the warpage exhibits

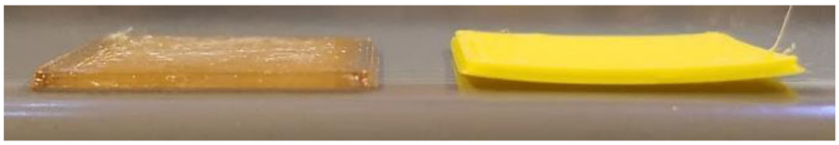

Fig. 11 Validation parts were printed using PPS and PP. FDM was used to fabricate 20 mm × 20 mm × 1 mm parts with PPS (left) and PP (right). The PPS part exhibited no visible warpage and remained adhered to the build platform for the duration of printing. The PP part warped and separated from the build platform during printing

conjunction with another material parameter. Thermal conductivity appeared to have a more significant impact on warpage when combined with effects from CTE. When modifying CTE and heat capacity together, the warpage seen was slightly larger than what was seen with CTE alone. However, it did not appear that the contribution from heat capacity increases when combined with thermal conductivity.

Based on the results seen by varying the material parameters of PPS to values of PP, additional values for the CTE, thermal conductivity, and Young's modulus were explored based on work done with polymer composites. An additional CTE value was used to confirm its direct scaling with warpage. Additional values for thermal conductivity and Young's modulus were chosen in order to assess if different values could more significantly affect the warpage of PPS.

Fillers have been used in various polymer systems to modify the thermal and mechanical properties of the combined system, or polymer composite [34]. Fillers in polymer composites can have various structures, such as particles or small fibers, and can be used in various loading amounts. Both inorganic and organic fillers have been employed such as carbon nanotubes, metal powders, cellulose nanocrystals, and glass fiber.

The CTE has been lowered by fabricating polymer composites with inorganic fillers with low thermal expansion values. Specifically, the addition of aluminum nitride (AIN) lowered the CTE and simultaneously increased the thermal conductivity of polyethylene polymer composites [35]. Lee et al. [35] showed a decrease in the CTE of polyethylene from 198 to 31.7 ppm/°C with the use of surface-treated AIN fillers. This value is significantly lower than the values for PPS and PP. A CTE value of 31.7 ppm/°C was used in the process simulation models for PPS.

The thermal conductivity of polymers is lower than the thermal conductivity of metals and many other inorganic materials. The thermal conductivity of polymers is typically in the range of 0.1 to 0.5 W/(m-K) while metals can have values as much as 3 orders of magnitude higher [34]. The thermal conductivity of polymers can be increased through the use of fillers with high thermal conductivities, such as metal or carbon fillers. Carbon nanotubes have attracted much interest as a filler for this purpose due to their high thermal conductivity (theoretically > 6000 W/m-K) [36]. Although the carbon nanotubes do not increase the thermal conductivity of polymer matrices as much as predicted by the rule of mixtures, the thermal conductivity of polymer composites has been doubled with the introduction of carbon nanotubes [37]. Based on this possibility, the thermal conductivity value for PPS was doubled and used in the simulation model with the other PPS material parameters.

The addition of particles to polymers can increase the Young's modulus of the polymer matrix. The use of various discontinuous organic, and inorganic fillers have been studied for this purpose and the effect of filler loading on

Table 4 Warpage of PPS simulation models with adjusted material parameters

PP parameter used with PPS simulation model	Warpage (mm)	$\frac{Parameter_{PP}}{Parameter_{PPS}}$	$\frac{Warpage_{parameter}}{Warpage_{PPS}}$
Coefficient of thermal expansion	0.050	2.98	2.98
Thermal conductivity	0.017	0.69	1.01
Heat capacity	0.017	1.92	1.00
Young's modulus	0.017	0.39	1.00

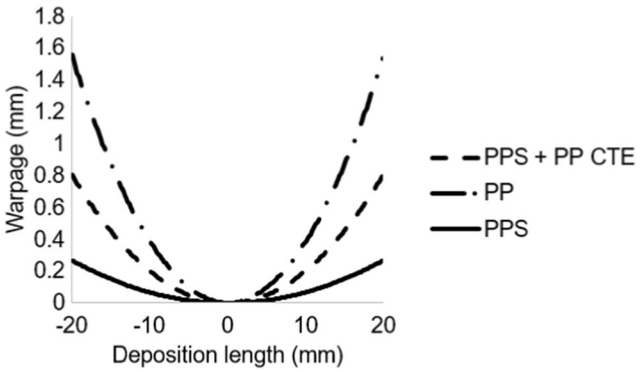

Fig. 12 Warpage vs. deposition length plots for PP, PPS, and CTE-modified PPS. The warpage value obtained using the process simulation models was used to extrapolate the warpage values at other deposition lengths. The PP simulation model exhibits more warpage than both the PPS simulation model and the PPS simulation model that used the CTE of PP.

Table 5 Warpage of PPS simulation models with multiple adjusted material parameters

PP parameter used with PPS simulation model	Warpage (mm)	$\frac{Warpage_{parameter}}{Warpage_{PPS}}$
Coefficient of thermal expansion + thermal conductivity	0.051	3.04
Coefficient of thermal expansion + heat capacity	0.050	2.99
Thermal conductivity + heat capacity	0.017	1.01
Coefficient of thermal expansion + thermal conductivity + heat capacity	0.051	3.03

the modulus can be modeled using the Guth-Gold model given in Eq. 6.

$$\frac{E}{E_s} = \left(1 + 2.5\varphi + 14.1\varphi^2\right) \tag{6}$$

where E_s is the modulus of the polymer and ϕ is the filler volume fraction [38]. The use of AIN particles in polyvinylidene fluoride increased the modulus from 2.2 to 15.51 GPa [39]. This value is much larger than the Young's modulus of PP and PPS. A Young's modulus value of 15 GPa was used in the simulation model with the other PPS material parameters.

Based on previous work with polymer composites, new values of CTE, thermal conductivity, and Young's modulus were used in the PPS process simulation models to further examine the effect of these material properties on part warpage. Table 6 shows the new material parameters used in the PPS simulation models, how they compare to the original material parameters, and how the warpage of the models was changed based on those values.

The warpage value obtained from the simulation using the additional CTE value confirmed that the warpage directly scales with CTE. Even though the thermal conductivity was changed more significantly in this set of simulations, it still had a minimal effect on the part warpage. Doubling the thermal conductivity only decreased the warpage to 99% of its original value. Consistent with what was shown before, changing Young's modulus did not significantly affect the part warpage seen in the simulation.

Table 6 Warpage of PPS simulation models with additional adjusted material parameters

Adjusted parameter used with PPS simulation model	Warpage (mm)	$\frac{Parameter_{adjusted}}{Parameter_{PPS}}$	$\frac{Warpage_{adjusted}}{Warpage_{PPS}}$
Coefficient of thermal expansion	0.011	0.63	0.63
Thermal conductivity	0.017	2.00	0.99
Young's modulus	0.017	3.33	1.00

4 Conclusions

In this study, the FDM process was modeled in three phases: road 1 deposition and cooling, road 2 deposition and cooling, and residual stress and warpage. The results seen in the deposition and cooling of two polymer FDM roads were consistent with process simulation models conducted previously. The temperature distribution for PPS was larger than that seen in PP and the observed cooling rates were larger. These differences were attributed to different deposition temperatures, lengths, and speeds. In the PPS process simulation, a higher deposition temperature, longer length, and slower deposition speed were used which resulted in larger thermal gradients throughout the FDM part.

The difference in warpage between PP and PPS experimental parts was investigated using the process simulation models. Various material parameters of PPS were adjusted to the values for PP to determine their effect on part warpage:

- Decreasing the CTE decreased part warpage by the same factor.
- Changing the thermal conductivity did not appear to have a significant effect on part warpage.
- Changing heat capacity did not appear to have a significant effect on part warpage.
- Changing the Young's modulus did not appear to have a significant effect on part warpage.

Additional values for the CTE, thermal conductivity, and Young's modulus were investigated for the PPS simulation models based on existing methods used to modify these values in polymer composites. The addition of fillers has shown to decrease the CTE, increase the thermal conductivity, and increase the Young's modulus. These modifications all led to a decrease in FDM part warpage in the simulation models. Overall, these process simulation models provide insight into which material properties most affect FDM part warpage. In addition, they provide a means to determine how fillers used in polymer composites could affect their performance in the FDM process.

Acknowledgements The authors gratefully acknowledge funding from Kimberly-Clark Corporation and donation of PPS from Technical Polymers for the capillary rheology experiments.

Funding This study was funded by Kimberly-Clark Corporation.

Compliance with ethical standards

Conflict of interest The authors declare that they have no conflict of interest.

References

1. Gibson I, Rosen DW, Stucker B (2005) Additive manufacturing technologies: rapid prototyping to direct digital manufacturing, 2nd edn. Springer, Berlin. https://doi.org/10.1007/978-1-4419-1120-9
2. Gao W, Zhang YB, Ramanujan D, Ramani K, Chen Y, Williams CB, Wang CCL, Shin YC, Zhang S, Zavattieri PD (2015) The status, challenges, and future of additive manufacturing in engineering. Comput Aided Design 69:65–89. https://doi.org/10.1016/j.cad.2015.04.001
3. Turner BN, Strong R, Gold SA (2014) A review of melt extrusion additive manufacturing processes: I. Process design and modeling. Rapid Prototyp J 20(3):192–204. https://doi.org/10.1108/rpj-01-2013-0012
4. Dawoud M, Taha I, Ebeid SJ (2016) Mechanical behaviour of ABS: an experimental study using FDM and injection moulding techniques. J Manuf Process 21:39–45. https://doi.org/10.1016/j.jmapro.2015.11.002
5. Lee J, Huang A (2013) Fatigue analysis of FDM materials. Rapid Prototyp J 19(4):291–299. https://doi.org/10.1108/13552541311323290
6. Ziemian C, Sharma M, Ziemian S (2012) Anisotropic mechanical properties of ABS parts fabricated by fused deposition modelling. In: Gokcek M (ed) Mechanical Engineering. INTECH. https://doi.org/10.5772/34233
7. Rubinstein M, Colby RH (2003) Polymer physics. Oxford, New York
8. Painter PC, Coleman MM (2008) Essentials of polymer science and engineering. DEStech Publications, Inc, Lancaster
9. De Santis F, Pantani R, Speranza V, Titomanlio G (2010) Analysis of shrinkage development of a semicrystalline polymer during injection molding. Ind Eng Chem Res 49(5):2469–2476. https://doi.org/10.1021/ie901316p
10. Shofner ML, Lozano K, Rodriguez-Macias FJ, Barrera EV (2003) Nanofiber-reinforced polymers prepared by fused deposition modeling. J Appl Polym Sci 89(11):3081–3090. https://doi.org/10.1002/app.12496
11. Zhong WH, Li F, Zhang ZG, Song LL, Li ZM (2001) Short fiber reinforced composites for fused deposition modeling. Mat Sci Eng A Struct 301(2):125–130. https://doi.org/10.1016/S0921-5093(00)01810-4
12. Tekinalp HL, Kunc V, Velez-Garcia GM, Duty CE, Love LJ, Naskar AK, Blue CA, Ozcan S (2014) Highly oriented carbon fiber-polymer composites via additive manufacturing. Compos Sci Technol 105:144–150. https://doi.org/10.1016/j.compscitech.2014.10.009
13. Ning FD, Cong WL, Qiu JJ, Wei JH, Wang SR (2015) Additive manufacturing of carbon fiber reinforced thermoplastic composites using fused deposition modeling. Compos Part B Eng 80:369–378. https://doi.org/10.1016/j.compositesb.2015.06.013
14. Quan ZZ, Wu A, Keefe M, Qin XH, JY Y, Suhr J, Byun JH, Kim BS, Chou TW (2015) Additive manufacturing of multidirectional preforms for composites: opportunities and challenges. Mater Today 18(9):503–512. https://doi.org/10.1016/j.mattod.2015.05.001
15. Kumar S, Kruth JP (2010) Composites by rapid prototyping technology. Mater Design 31(2):850–856. https://doi.org/10.1016/j.matdes.2009.07.045
16. Gray RW, Baird DG, Bohn JH (1998) Effects of processing conditions on short TLCP fiber reinforced FDM parts. Rapid Prototyp J 4(1):14–25. https://doi.org/10.1108/13552549810197514
17. Korpela J, Kokkari A, Korhonen H, Malin M, Narhi T, Seppala J (2013) Biodegradable and bioactive porous scaffold structures prepared using fused deposition modeling. J Biomed Mater Res B 101b(4):610–619. https://doi.org/10.1002/jbm.b.32863
18. Gray RW, Baird DG, Bohn JH (1998) Thermoplastic composites reinforced with long fiber thermotropic liquid crystalline polymers for fused deposition modeling. Polym Composite 19(4):383–394. https://doi.org/10.1002/pc.10112
19. Carneiro OS, Silva AF, Gomes R (2015) Fused deposition modeling with polypropylene. Mater Design 83:768–776. https://doi.org/10.1016/j.matdes.2015.06.053
20. Love LJ, Kunc V, Rios O, Duty CE, Elliott AM, Post BK, Smith RJ, Blue CA (2014) The importance of carbon fiber to polymer additive manufacturing. J Mater Res 29(17):1893–1898. https://doi.org/10.1557/jmr.2014.212
21. DeNardo NM (2016) Additive manufacturing of carbon fiber-reinforced thermoplastic composites. Dissertation, Purdue University
22. Boparai KS, Singh R, Fabbrocino F, Fraternali F (2016) Thermal characterization of recycled polymer for additive manufacturing applications. Compos Part B Eng 106:42–47. https://doi.org/10.1016/j.compositesb.2016.09.009
23. Watanabe N, Shofner M, Treat N, Rosen D (2016) A model for residual stress and part warpage prediction in material extrusion with application to polypropylene. In: 2016 Annual International Solid Freeform Fabrication Symposium, Austin
24. Jog JP, Nadkarni VM (1985) Crystallization kinetics of polyphenylene sulfide. J Appl Polym Sci 30(3):997–1009. https://doi.org/10.1002/app.1985.070300310
25. Lovinger AJ, Padden FJ, Davis DD (1988) Structure of poly(p-phenylene sulfide). Polymer 29(2):229–232. https://doi.org/10.1016/0032-3861(88)90326-6
26. Agarwala MK, Jamalabad VR, Langrana NA, Safari A, Whalen PJ, Danforth SC (1996) Structural quality of parts processed by fused deposition. Rapid Prototyp J 2(4):4–19. https://doi.org/10.1108/13552549610732034
27. Bellini A, Guceri S, Bertoldi M (2004) Liquefier dynamics in fused deposition. J Manuf Sci E T ASME 126(2):237–246. https://doi.org/10.1115/1.1688377
28. Dynisco (2016) Capillary rheometer (LCR7000 series). http://wwwdyniscocom/capillary-rheometer–lcr-7000-series. Accessed 8 May 2017
29. Quadrantplasics.com Techtron PPS - Quadrant. http://www.quadrantplastics.com/na-en/products/engineering-plastics/advanced-325-425-f/techtron-R-pps.html. Accessed 8 May 2017
30. Critical surface tension and contact angle with water for various polymers. https://www.accudynetest.com/polytable_03.html. Accessed 14 Oct 2017
31. HYREL system 30. http://www.hyrel3d.com/. Accessed 8 May 2017
32. Repetier homepage. http://www.repetier.com/. Accessed 8 May 2017
33. Hodgson G Slic3r manual. http//www.manual.slic3r.org/intro/overview. Accessed 8 May 2017
34. Tsou A, Waddell W (2002) Fillers. Encyclopedia of polymer science and technology. Wiley, New York
35. Lee GW, Park M, Kim J, Lee JI, Yoon HG (2006) Enhanced thermal conductivity of polymer composites filled with hybrid filler. Compos Part A Appl Sci Manuf 37(5):727–734. https://doi.org/10.1016/j.compositesa.2005.07.006
36. Moniruzzaman M, Winey KI (2006) Polymer nanocomposites containing carbon nanotubes. Macromolecules 39(16):5194–5205. https://doi.org/10.1021/ma060733p
37. Han ZD, Fina A (2011) Thermal conductivity of carbon nanotubes and their polymer nanocomposites: a review. Prog Polym Sci 36(7):914–944. https://doi.org/10.1016/j.progpolymsci.2010.11.004
38. Guth E (1945) Theory of filler reinforcement. J Appl Phys 16(1):20–25. https://doi.org/10.1063/1.1707495
39. Xu YS, Chung DDL, Mroz C (2001) Thermally conducting aluminum nitride polymer-matrix composites. Compos Part A Appl Sci Manuf 32(12):1749–1757. https://doi.org/10.1016/S1359-835x(01)00023-9